J|A|C|S
ARTICLES
Published on Web 05/01/2007

Determination of Radical Re-encounter Probability Distributions from Magnetic Field Effects on Reaction Yields

Christopher T. Rodgers,[†] Stuart A. Norman,[†] Kevin B. Henbest,[†,‡] Christiane R. Timmel,[*,‡] and P. J. Hore[*,†]

Contribution from the Department of Chemistry, University of Oxford, Physical and Theoretical Chemistry Laboratory, South Parks Road, Oxford, OX1 3QZ, United Kingdom, and Department of Chemistry, University of Oxford, Inorganic Chemistry Laboratory, South Parks Road, Oxford, OX1 3QR, United Kingdom

Received November 16, 2006; E-mail: peter.hore@chem.ox.ac.uk; christiane.timmel@chem.ox.ac.uk

Abstract: Measurements are reported of the effects of 0−23 mT applied magnetic fields on the spin-selective recombination of $Py^{\bullet-}$ and $DMA^{\bullet+}$ radicals formed in the photochemical reaction of pyrene and *N,N*-dimethylaniline. Singlet ↔ triplet interconversion in [$Py^{\bullet-}$ $DMA^{\bullet+}$] radical pairs is probed by investigating combinations of fully protonated and fully deuterated reaction partners. Qualitatively, the experimental $B_{1/2}$ values for the four isotopomeric radical pairs agree with predictions based on the Weller equation using known hyperfine coupling constants. The amplitude of the "low field effect" (LFE) correlates well with the ratio of effective hyperfine couplings, $\langle a_{DMA}\rangle/\langle a_{Py}\rangle$. An efficient method is introduced for calculating the spin evolution of [$Py^{\bullet-}$ $DMA^{\bullet+}$] radical pairs containing a total of 18 spin-$^1/_2$ and spin-1 magnetic nuclei. Quantitative analysis of the magnetic field effects to obtain the radical re-encounter probability distribution $f(t)$—a highly ill-posed and underdetermined problem—is achieved by means of Tikhonov and maximum entropy regularization methods. The resulting $f(t)$ functions are very similar for the four isotopomeric radical pairs and have significant amplitude between 2 and 10 ns after the creation of the geminate radical pair. This interval reflects the time scale of re-encounters that are crucial for generating the magnetic field effect. Computer simulations of generalized radical pairs containing six spin-$^1/_2$ nuclei show that Weller's equation holds approximately only when the radical pair recombination rate is comparable to the two effective hyperfine couplings and that a substantial LFE requires, but is not guaranteed by, the condition that the two effective hyperfine couplings differ by more than a factor of 5. In contrast, for very slow recombination, essentially any radical pair should show a significant LFE.

1. Introduction

Magnetic fields can alter the rates and yields of chemical reactions that proceed via spin-correlated radical pair intermediates and so provide information on the structures, dynamics, kinetics, and reactivity of free radicals.[1−3] Chemical magnetosensitivity via the radical pair mechanism (RPM) requires the following sequence of events: first, creation of a pair of radicals, with correlated electron spins, in a pure singlet (S) or pure triplet (T) state; second, coherent evolution of the radical pair between the near-degenerate S and T spin states; and third, reaction of the S and T radical pairs to form different products (or the same product at different rates). It is during the second of these steps that the magnetic field acts, via the electron Zeeman interaction, altering the extent and frequency of S ↔ T interconversion and hence the relative yields of reaction products and/or the lifetime of the radical pair. RPM magnetic field effects are thus kinetic, rather than thermodynamic, in origin and may be detected for magnetic fields whose Zeeman energies are much smaller than the average thermal energy per molecule, k_BT.

As the only well-established mechanism by which low-energy electromagnetic radiation can affect chemical processes, the RPM has featured in debates on the possible adverse health effects of the very weak fields emitted by electrical equipment and power transmission lines[4−6] and has been proposed as a mechanism for the magnetic compass sense of migratory birds.[7,8] In both cases, the magnetic fields involved are weaker than 1 mT such that, for typical organic free radicals, the magnetic electron−nuclear hyperfine interactions in the radical pair are larger than the electron Zeeman interactions. Such systems may demonstrate a "low field effect"[9−16] (LFE), which leads to a

[†] Physical and Theoretical Chemistry Laboratory.
[‡] Inorganic Chemistry Laboratory.

(1) Steiner, U. E.; Ulrich, T. *Chem. Rev.* **1989**, *89*, 51−147.
(2) Woodward, J. R. *Prog. React. Kinet. Mech.* **2002**, *27*, 165−207.
(3) Brocklehurst, B. *Chem. Soc. Rev.* **2002**, *31*, 301−311.
(4) Brocklehurst, B.; McLauchlan, K. A. *Int. J. Radiat. Biol.* **1996**, *69*, 3−24.
(5) Swanson, J.; Kheifets, L. *Radiat. Res.* **2006**, *165*, 470−478.
(6) NRPB report of the Advisory Group on Non-ionising Radiation, Chairman Sir Richard Doll, ELF Electromagnetic Fields and the Risk of Cancer, 2001, Chapter 8, paragraph 2.
(7) Schulten, K.; Swenberg, C. E.; Weller, A. *Z. Phys. Chem. NF* **1978**, *111*, 1−5.
(8) Ritz, T.; Adem, S.; Schulten, K. *Biophys. J.* **2000**, *78*, 707−718.
(9) Brocklehurst, B. *J. Chem. Soc., Faraday Trans. II* **1976**, *72*, 1869−1884.
(10) Timmel, C. R.; Till, U.; Brocklehurst, B.; McLauchlan, K. A.; Hore, P. J. *Mol. Phys.* **1998**, *95*, 71−89.
(11) Eveson, R. W.; Timmel, C. R.; Brocklehurst, B.; Hore, P. J.; McLauchlan, K. A. *Int. J. Radiat. Biol.* **2000**, *76*, 1509−1522.

10.1021/ja068209l CCC: $37.00

Scheme 1. Essential Steps in the Photoinduced Reaction of Pyrene and *N,N*-Dimethylaniline via the Radical Pair State [$Py^{\bullet-}$ $DMA^{\bullet+}$] which is Responsible for the Magnetic Field Sensitivity of the Exciplex Fluorescence

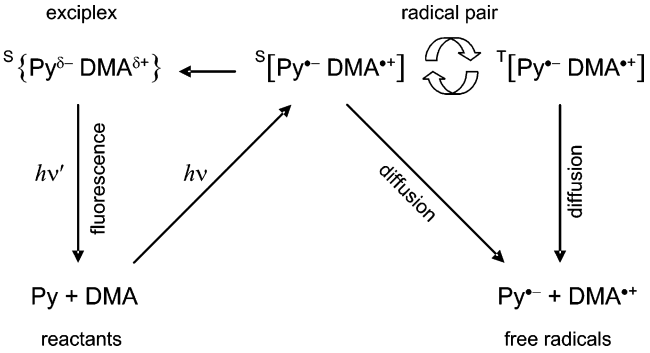

decrease in the fraction of singlet-born radical pairs that recombine via the S state (and, conversely, an increase for triplet-born pairs). When present, the LFE dominates the response to applied magnetic fields that are weaker than the hyperfine interactions.

There have been several attempts to predict the circumstances in which an LFE may be expected.[10,13,17] The LFE is characterized by two key parameters (stated here for a singlet-born radical pair): the strength of the applied magnetic field at which the yield of the product formed from the S state of the radical pair (the "S-product") is at a minimum—the "low field position"—and the extent of the decrease in S-product yield at this low field position compared to that without a magnetic field—the "low field depth". On the one hand, theory predicts that, for very slow recombination reactions, essentially any radical pair can be expected to show a significant LFE irrespective of the hyperfine couplings, and their distribution, in the radicals.[10,17] However, experimental observations and other theoretical approaches[13] suggest that the LFE is weak unless one, but not both, of the radicals has a small effective hyperfine interaction. The two predictions rely on different assumptions about the nature of the recombination kinetics in the radical pair and are thus not necessarily mutually incompatible. In studies of free radical reactions and in the more exotic contexts of health hazards and animal magnetoreception, it is important to understand how the two parameters depend on the chemical and magnetic properties of the radicals and which, if either, of the two limiting cases mentioned above holds in any given situation. These questions, among others, are addressed here.

As the magnetic field strength is increased, the LFE gradually gives way to the "conventional" magnetic field effect (MFE) on the relative product yields and/or radical pair lifetime. This change occurs as the Zeeman interaction energy increases and comes to dominate the hyperfine interactions; it can be understood in terms of the detailed interplay of the two types of magnetic interaction and their effects on S ↔ T interconversion.[1,10] The MFE has a phase that is opposite to that of the LFE, i.e., an increase in S-product yield for a singlet-born radical pair. The characteristics of both LFE and MFE also depend on the relative translational motion of the radicals in solution. At the instant of their creation, the two radicals that comprise a geminate pair are usually sufficiently close to one another that their mutual exchange interaction is large enough to lock the pair into its initial S or T state. Only when the radicals have separated to a point where the exchange is comparable to the hyperfine and Zeeman interactions (typically 1.0−1.5 nm), can S ↔ T interconversion start. For the magnetic field to affect the product yield, the radicals have then to diffuse back together ("re-encounter") in order to be able to recombine in a spin-selective fashion, usually from the S state. In this respect, the origin of magnetic field effects parallels that of chemically induced dynamic electron and nuclear polarization, CIDEP and CIDNP, which also require a period of exchange-free S ↔ T interconversion prior to a diffusive re-encounter.[18−23] A simple way of modeling these trajectories is in terms of a re-encounter probability distribution $f(t)$,[20,24] as described below.

Traditionally, two approaches have been taken to quantify MFE data. One is based on the observation that most MFE responses are approximately sigmoidal. The principal variation observed for different radical pairs may therefore be quantified by measuring the zero-field and high-field (saturation) values of the product yield and hence the magnetic field strength, $B_{1/2}$, corresponding to a product yield mid-way between these limits.[25−27] The other approach involves model-fitting computer simulations of the magnetic field response using a set of magnetic interaction parameters (*g*-values, hyperfine couplings, etc.) and a model for the diffusive motion of the radicals. This procedure is most successful when the majority of the parameters in the model are independently known, e.g., *g*-values and hyperfine coupling constants from EPR or ENDOR spectra or from *ab initio* calculations.

To determine more clearly the roles played by spin-dynamics and diffusional motion, we have measured the effect of an applied magnetic field on the radical ion pair [$Py^{\bullet-}$ $DMA^{\bullet+}$] formed in the photochemical reaction of pyrene (Py) with *N,N*-dimethylaniline (DMA) in a viscous solvent. The exciplex fluorescence produced by this reaction is strong and allows sensitive measurements of the S-product yield.[28,29] To allow reliable separation of spin and motion effects, data have been recorded for combinations of fully protonated or fully deuterated reactants (Py-h_{10}, Py-d_{10}, DMA-h_{11}, DMA-d_{11}) to obtain four isotopomeric radical pairs. It seems reasonable to suppose that deuteration has little effect on the diffusive motion of the radicals or on their reactivity but that it will dramatically alter the hyperfine interactions and thus the S ↔ T interconversion, principally via the 6.5-fold difference in the magnetic moments

(12) Batchelor, S. N.; Kay, C. W. M.; McLauchlan, K. A.; Shkrob, I. A. *J. Phys. Chem.* **1993**, *97*, 13250−13258.
(13) Stass, D. V.; Lukzen, N. N.; Tadjikov, B. M.; Molin, Y. N. *Chem. Phys. Lett.* **1995**, *233*, 444−450.
(14) Stass, D. V.; Tadjikov, B. M.; Molin, Y. N. *Chem. Phys. Lett.* **1995**, *235*, 511−516.
(15) Sacher, M.; Grampp, G. *Ber. Bunsen. Phys. Chem.* **1997**, *101*, 971−974.
(16) Saik, V. O.; Ostafin, A. E.; Lipsky, S. *J. Chem. Phys.* **1995**, *103*, 7347−7358.
(17) Till, U.; Timmel, C. R.; Brocklehurst, B.; Hore, P. J. *Chem. Phys. Lett.* **1998**, *298*, 7−14.
(18) Kaptein, R.; Oosterhoff, L. J. *Chem. Phys. Lett.* **1969**, *4*, 195−197.
(19) Kaptein, R. *J. Am. Chem. Soc.* **1972**, *94*, 6251−6262.
(20) Adrian, F. J. *J. Chem. Phys.* **1971**, *54*, 3912−3917.
(21) Closs, G. L. *J. Am. Chem. Soc.* **1969**, *91*, 4552−4554.
(22) Closs, G. L.; Trifunac, A. D. *J. Am. Chem. Soc.* **1970**, *92*, 2183−2184.
(23) Pedersen, J. B.; Freed, J. H. *J. Chem. Phys.* **1973**, *58*, 2746−2762.
(24) Noyes, R. M. *J. Chem. Phys.* **1954**, *22*, 1349−1359.
(25) Justinek, M.; Grampp, G.; Landgraf, S.; Hore, P. J.; Lukzen, N. N. *J. Am. Chem. Soc.* **2004**, *126*, 5635−5646.
(26) Weller, A.; Nolting, F.; Staerk, H. *Chem. Phys. Lett.* **1983**, *96*, 24−27.
(27) Henbest, K. B.; Athanassiades, E.; Maeda, K.; Kuprov, I.; Hore, P. J.; Timmel, C. R. *Mol. Phys.* **2006**, *104*, 1789−1794.
(28) Weller, A.; Staerk, H.; Treichel, R. *Faraday Discuss.* **1984**, 271−278.
(29) Woodward, J. R.; Timmel, C. R.; McLauchlan, K. A.; Hore, P. J. *Phys. Rev. Lett.* **2001**, *87*, 077602.

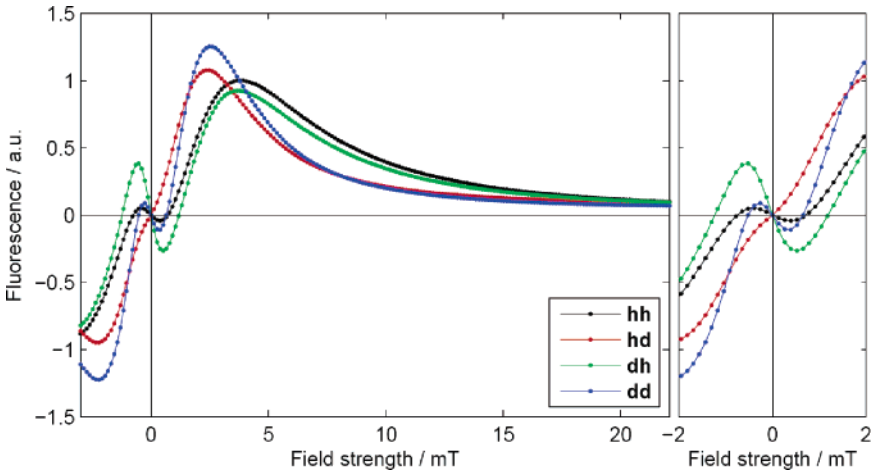

Figure 1. First-derivative magnetic field effect on the photochemical reaction of pyrene and *N*,*N*-dimethylaniline detected as the intensity of the modulated fluorescence of the exciplex formed from the singlet [$Py^{\bullet-}$ $DMA^{\bullet+}$] radical pair. Data are shown for the four isotopomeric radical pairs described in the text: **hh** (black), **hd** (red), **dh** (green), **dd** (blue). The panel on the right is an expansion of the low field region. In both panels, the experimental data points (filled circles) are linked by lines to guide the eye.

of ^1H and ^2H nuclei. A novel approach is introduced for interpreting the LFE and MFE data in such a reaction system. Using Tikhonov and maximum entropy regularization techniques, we show that it is possible to extract an *empirical* re-encounter probability distribution function for each isotopomeric radical pair directly from the experimental data.

2. Experimental Methods

A simplified reaction scheme for the photoinduced electron-transfer reaction between Py and DMA is shown in Scheme 1. Both S and T pairs can diffuse out of the geminate solvent cage to form free radicals, but only S pairs can recombine to produce a fluorescent exciplex. An applied magnetic field modifies the S ↔ T interconversion, alters the fraction of radical pairs that form exciplexes, and hence changes the fluorescence intensity.

Singlet [$Py^{\bullet-}$ $DMA^{\bullet+}$] radical ion pairs were generated by continuous UV irradiation using a 300 W Xe arc lamp (Oriel 66011) with a power supply (Oriel 68811) which delivered approximately constant light intensity across the 300−800 nm range. The light was passed through a water filter to remove the infrared components, through a UV short-pass filter (Andover 345FG01−50; 50% cutoff at 345 nm) and then directed to the sample via a liquid-filled light guide. The fluorescence was collected at 90° to the incident beam, filtered (548 nm filter; 100 nm bandwidth), and transmitted via a light guide to a photomultiplier tube (Hamamatsu R928 mounted on a Hamamatsu C6271 high voltage power supply unit). A variable resistor allowed manual adjustment of the bias voltage across the photomultiplier whose output was sent to an analogue lock-in amplifier (Stanford Research Systems SR510) which was connected to a personal computer and controlled using LabVIEW software.

One output from the lock-in amplifier was used to drive the power supply for the static-field coils, generating 0.0−0.6 A, corresponding to a maximum field of 26 mT. A second set of coils was fed with both fixed and audio frequency currents, the latter under the control of the lock-in amplifier; the former was manually controlled and provided a static field of up to 8 mT antiparallel to that produced by the static-field coils. The amplitude of the 379 Hz audio frequency field modulation was adjustable in the range 0−2 mT; the resulting modulations in the exciplex fluorescence were detected as described above. The net applied field is the sum of the contributions from the two sets of coils and was typically swept from −3 mT to +23 mT, with a modulation amplitude of 1.75 mT. The modulation technique results in a signal that is proportional to the first derivative of the exciplex fluorescence intensity with respect to the strength of the applied magnetic field. A modulation depth of 1.75 mT was found in preliminary studies to optimize the signal-to-noise for field strengths around the low field region effect without changing the shape of the signal excessively. Simulations of the field dependence of the singlet yield were used to test for side effects of modulation. It was found that moderate amounts of distortion arising from field modulation did not substantially degrade the quality of the recovered re-encounter probability distribution (see below).

Magnetic field effects were measured for solutions of 1.0 mM pyrene (Py-h_{10} or Py-d_{10}) and 20 mM *N*,*N*-dimethylaniline (DMA-h_{11} or DMA-d_{11}) in a 1:4 mixture of dimethylformamide (DMF) and tetrahydrofuran (THF). Samples were sonicated for 30 min to aid dissolution of the pyrene and to ensure good mixing. Deoxygenation by bubbling with nitrogen was found to have an insignificant effect on the measured signal strength and shape. The data presented for the four isotopomeric mixtures were each averages of three separate measurements on three 3 mL samples. As far as possible, experimental conditions for the isotopomer combinations were identical; the relative amplitudes of the four data sets are therefore significant. Chemicals and solvents were used as received: Py-h_{10} (Aldrich; 98%), Py-d_{10} (Cambridge Isotope Laboratories, Inc; 98%), DMA-h_{11} (Fluka; >99.5%), DMA-d_{11} (Cambridge Isotope Laboratories, Inc; >98%), THF (Sigma-Aldrich; 99.5+%, spectrophotometric grade), and DMF (Sigma-Aldrich; ≥99.8%, ACS reagent, spectrophotometric grade).

3. Qualitative Analysis of Magnetic Field Effects

The dependence of the intensity of the modulated fluorescence on the strength of the applied magnetic field ($-3 < B < 23$ mT) is shown in Figure 1 for the four [$Py^{\bullet-}$ $DMA^{\bullet+}$] isotopomers. For brevity, we will refer to the four isotopomer combinations as "**hh**" ([Py-$h_{10}^{\bullet-}$ DMA-$h_{11}^{\bullet+}$]), "**hd**" ([Py-$h_{10}^{\bullet-}$ DMA-$d_{11}^{\bullet+}$]), "**dh**" ([Py-$d_{10}^{\bullet-}$ DMA-$h_{11}^{\bullet+}$]), and "**dd**" ([Py-$d_{10}^{\bullet-}$ DMA-$d_{11}^{\bullet+}$]). The use of field modulation and the consequent detection of the field derivative of the fluorescence intensity mean that the data should be antisymmetric around $B = 0$ mT, as is indeed observed.

Several features are immediately obvious. All four data sets have broadly similar amplitudes; all except **hd** show an LFE, the negative-going region between 0 and ∼1 mT; and all four show saturation behavior at magnetic fields greater than about 20 mT. Such observations are common to a great many magnetic field effect measurements[9−16] and have motivated the use of empirical parameters for their qualitative analysis. The pertinent

Table 1. Empirical Magnetic Field Effect Parameters and Effective Hyperfine Coupling Constants for [Py$^{\bullet-}$ DMA$^{\bullet+}$] Radical Pairs

isotopomer combination	hh	hd	dh	dd
experimental LFE depth[a]	0.15	–	1.54	0.35
experimental $B_{1/2}$/mT	6	4	7	4
calculated[b] $\langle a_{DMA}\rangle/\langle a_{Py}\rangle$	3.2	1.8	12.9	7.3
calculated[b] $B_{1/2}$/mT	5.0	2.8	5.6	3.0

[a] Arbitrary units. [b] Calculated using the data in Table 2 and eqs 1 and 2.

parameters are the LFE depth, defined here as the integral over the negative-going region of the data around zero field, and the half-saturation field[26] $B_{1/2}$, defined as the magnetic field at which the integrated signal reaches exactly one-half of the integral from $B = 0$ mT to $B = \infty$ mT. Table 1 gives the values of these parameters measured from the data in Figure 1.

In an attempt to shed light on these empirical parameters and their dependence on the isotopic composition of the two radicals, we have calculated the magnetic field responses for an ensemble of 12 737 radical pairs. Each member of the ensemble contained six spin-$^1/_2$ nuclei with distinct hyperfine coupling constants, three on each radical. For each radical, these were chosen as follows: (i) the effective hyperfine coupling constant (defined as in eq 1, below) was chosen at random from a uniform distribution between 0 and 1.5 mT; (ii) three numbers were chosen at random from independent Gaussian distributions with zero mean, and (iii) these three numbers were scaled to give a set of hyperfine couplings consistent with the effective hyperfine coupling constant chosen in the first step. This method of selecting the hyperfine coupling constants ensures that a range of effective hyperfine couplings is covered and that individual hyperfine coupling constants are chosen without bias from among those compatible with the effective hyperfine coupling constant. After this, magnetic field responses were calculated for each member of the ensemble using an exponential distribution of re-encounter lifetimes (the "exponential model"[9,18]) with the rate constant k varying over many orders of magnitude. Comparison of the LFE depth and $B_{1/2}$, measured from the calculated magnetic field dependence for each RP, with the corresponding hyperfine couplings and rate constants allows us to establish some "rules of thumb". (See the Supporting Information for illustrative results.)

Perhaps the most significant result to come from these computations is that the factors controlling the LFE depth and $B_{1/2}$ differ quite markedly between systems where the exponential model rate constant k is smaller than, comparable to, or greater than the effective hyperfine coupling constants in each radical defined, following Schulten,[30] as

$$\langle a_X\rangle = \sqrt{\frac{4}{3}\sum_i a_{iX}^2\, I_{iX}(I_{iX}+1)} \qquad (1)$$

with I_{iX} being the spin quantum number of nuclear spin i with hyperfine coupling constant a_{iX} in radical X.[31]

(30) Schulten, K.; Bittl, R. *J. Chem. Phys.* **1986**, *84*, 5155−5161.
(31) The literature contains conflicting definitions of the effective (or average) hyperfine coupling constant. We have chosen to use a definition incorporating a factor of 4/3 in order that the hyperfine energies of a one-proton radical pair are conserved when it is considered in terms of effective hyperfine coupling constants.

Table 2. Hyperfine Coupling Constants in Py$^{\bullet-}$ and DMA$^{\bullet+}$ Radicals[a]

species X	a_{1X}/mT	a_{2X}/mT	a_{3X}/mT	$\langle a_X\rangle$/mT[b]
Py-$h_{10}^{\bullet-}$ [c]	0.481 (4H)	0.212 (4H)	0.103 (2H)	1.061
Py-$d_{10}^{\bullet-}$ [e]	0.074 (4D)	0.033 (4D)	0.016 (2D)	0.267
DMA-$h_{11}^{\bullet+}$ [d]	1.180 (6H)	1.100 (1N)	0.520 (1H)	3.443
DMA-$d_{11}^{\bullet+}$ [e]	0.181 (6D)	1.100 (1N)	0.080 (1D)	1.941

[a] Hyperfine coupling constants are listed for the three groups of equivalent nuclei in each radical that have the largest couplings. H, D, and N indicate ^{1}H, ^{2}H, and ^{14}N. The number of equivalent nuclei in each group is given in parentheses. [b] Effective hyperfine coupling constant calculated using eq 1. [c] Hyperfine data taken from ref 33. [d] Hyperfine data taken from ref 34. [e] The ^{2}H couplings were obtained using $a_{deuterated}/a_{protonated} = \gamma_D/\gamma_H = 0.1535$.

For rate constants comparable to the effective hyperfine couplings constants, i.e., when $k \approx 5 \times 10^7$ s^{-1}, we find a substantial LFE depth only when the effective hyperfine coupling constant on one radical is much larger than that for the other radical. However, we also find the largest variation in LFE depth under these conditions. In other words, a substantial LFE depth requires, but is not guaranteed by, the condition that the two effective hyperfine couplings should differ by more than a factor of 5. This rule of thumb is consistent with the empirical observations of Molin and Stass and co-workers[13] and quite different from the behavior in the limit of long lifetimes (i.e., when k is much smaller than both of the effective hyperfine couplings).[10,17] We will return to this point below.

The half-saturation field $B_{1/2}$ is sometimes predicted using the formula

$$B_{1/2} = \sqrt{3}\,\frac{\langle a_A\rangle^2 + \langle a_B\rangle^2}{\langle a_A\rangle + \langle a_B\rangle} \qquad (2)$$

due to Weller[26,32] (A and B label the two radicals). Analysis of the calculated magnetic field effects for the ensemble of RPs described above again shows different behavior depending on the magnitude of the rate constant k relative to the effective hyperfine couplings. Equation 2 holds for the most part to within a factor of 2 at the intermediate rate constants considered here and may therefore be considered as a second rule of thumb. However, for faster or slower recombination the agreement is much less satisfactory (see Supporting Information).

Table 2 presents the three largest hyperfine coupling constants (a_{iX}) and the effective coupling constants ($\langle a_{Py}\rangle$ and $\langle a_{DMA}\rangle$) for each of the four radicals.[33,34] These values were used to determine the ratio of effective coupling constants and the value of $B_{1/2}$, using eq 2, for each radical pair (Table 1). Comparing these calculated values with the corresponding experimental results (also in Table 1), it is clear that the empirical parameters for the four radical pairs are indeed consistent with the rules of thumb outlined above. Specifically, the measured LFE depth increases as the two effective hyperfine couplings become more disparate and the measured $B_{1/2}$ corresponds reasonably well to the Weller formula.

The set of 12 737 simulated radical pairs also allows us to verify the theoretical prediction that essentially any radical pair

(32) The version of eq 2 given by Weller et al. has a leading factor of 2 instead of $\sqrt{3}$ because their version of eq 1 does not contain the 4/3 factor.
(33) Claridge, R. F.; Kirk, C. M.; Peake, B. M. *Aust. J. Chem.* **1973**, *26*, 2055−2058.
(34) Pobedimskii, B. G.; Buchachenko, A. L.; Neiman, M. B. *Russ. J. Phys. Chem.* **1968**, *42*, 748−751.

should have a significant LFE if the recombination and spin relaxation of the radicals are sufficiently slow.[10,17] In contrast to the result described above for $k \approx \langle a_A \rangle, \langle a_B \rangle$, all the radical pairs studied show substantial LFEs when $k \ll \langle a_A \rangle, \langle a_B \rangle$ irrespective of the relative sizes of the two effective hyperfine couplings (see Supporting Information). In addition, exponential model simulations of the magnetic field effects for the four isotopomeric radical pairs investigated here reveal LFE depths that mirror $\langle a_{DMA} \rangle / \langle a_{Py} \rangle$ when $k \approx \langle a_{DMA} \rangle, \langle a_{Py} \rangle$ (as found experimentally) but which are essentially independent of $\langle a_{DMA} \rangle$ and $\langle a_{Py} \rangle$ when $k << \langle a_{DMA} \rangle, \langle a_{Py} \rangle$.

Returning to Table 1, the agreement between the calculated effective hyperfine couplings and the empirical field effect parameters implies that the differences in the observed field effect curves shown in Figure 1 arise from changes in the spin dynamics via the isotope effect on the $^1H/^2H$ hyperfine interactions. However, it cannot be ruled out at this stage that the observed variations in LFE depth and $B_{1/2}$ arise from differences in the recombination rates of the isotopomeric radical pairs due, for example, to an isotope effect on the electron-transfer rates. We therefore proceed to a detailed quantitative analysis of the data in Figure 1.

4. Calculation of Magnetic Field Effects

The RPM provides the mechanistic basis for our quantitative interpretation of the data in Figure 1. The amplitude of the modulated exciplex fluorescence is assumed to be proportional to the first derivative with respect to magnetic field strength of the S-product yield, $d\Phi_S(B)/dB$. We further assume that this product yield may be written in terms of the singlet projection operator, $\hat{P}^S$, as[18]

$$\Phi_S(B) = \int_0^\infty \langle \hat{P}^S \rangle(B,t)\, f(t)\, dt \tag{3}$$

where $\langle \hat{P}^S \rangle(B,t)$ is the probability that the radical pair will be found in a singlet state for a given magnetic field strength B at a time t after the instant of radical pair creation, and $f(t)$ is the probability[24] that the radicals re-encounter at time t. A validation of this approach is presented in the Supporting Information. Equation 3 treats every singlet state re-encounter as reactive (i.e., a diffusion controlled reaction) and ignores the possibility of multiple re-encounters. Thus, after an unreactive (triplet state) re-encounter the radicals are assumed to separate, never to meet again. Our aim is to calculate $\partial \langle \hat{P}^S \rangle(B,t)/\partial B$ in order to be able to solve the integral equation that is the field-derivative of eq 3 to obtain an empirical re-encounter probability distribution $f(t)$ from the measured fluorescence signals.

We assume that the only significant spin interactions are the isotropic hyperfine interaction between the electron and nuclear spins in each radical and the isotropic Zeeman interaction of the two electron spins with the applied magnetic field. (Anisotropic interactions are efficiently averaged by molecular tumbling in solution; spin relaxation is insignificant during the short radical pair lifetime; g-value differences between the two radicals and nuclear Zeeman interactions are negligible at the magnetic field strengths of interest; the electron exchange and dipolar interactions are assumed to be negligible.) Thus, we write the spin Hamiltonian of the radical pair (in angular frequency units) as $\hat{H} = \hat{H}^A + \hat{H}^B$ where

$$\hat{H}^X = \sum_i a_{iX} \hat{\mathbf{S}}_X \cdot \hat{\mathbf{I}}_i - \gamma_e B \hat{S}_{Xz} \tag{4}$$

in which A and B label the two radicals, $\hat{\mathbf{S}}_X$ and $\hat{\mathbf{I}}_i$ are the electron and nuclear spin operators, respectively, γ_e is the electron magnetogyric ratio, and the magnetic field B is applied along the z-axis. The hyperfine coupling constants a_{iX} used in these calculations are given in Table 2.

Working in the density matrix formalism, we write the singlet probability as

$$\langle \hat{P}^S \rangle(B,t) = \mathrm{Tr}[\hat{\rho}(B,t)\hat{P}^S] \tag{5}$$

The density operator evolves from its initial singlet state under the influence of the Hamiltonian as

$$\hat{\rho}(B,t) = \hat{U}\hat{\rho}(0)\hat{U}^\dagger = \frac{1}{M}\hat{U}\hat{P}^S\hat{U}^\dagger \tag{6}$$

where M is the number of nuclear spin states and the propagator $\hat{U} = e^{-i\hat{H}t}$. Note that this procedure automatically includes the interconversion of the singlet state with all three triplet states, T_{+1}, T_0, and T_{-1}. Then, using $\hat{P}^S = (^1/_4)\hat{1} - \hat{\mathbf{S}}_A \cdot \hat{\mathbf{S}}_B$, we can calculate the spin evolution of the two radicals separately. Following Till et al.,[17] we obtain

$$\langle \hat{P}^S \rangle(B,t) = \frac{1}{4} + \frac{1}{M} \sum_{p,q=x,y,z} R^A_{pq}(t)\, R^B_{pq}(t) \tag{7}$$

in which

$$R^X_{pq}(t) = \mathrm{Tr}[\hat{S}_{Xp} e^{-i\hat{H}^X t}\, \hat{S}_{Xq} e^{i\hat{H}^X t}] \tag{8}$$

The latter expression is simplified by transforming to the eigenbasis of the Hamiltonian. We define

$$\tilde{H} = V^T \hat{H} V \text{ and } \tilde{S}_{Xp} = V^T \hat{S}_{Xp} V \tag{9}$$

where V is the real, orthogonal matrix of eigenvectors of $\hat{H}$, and $\tilde{H}$ is the real, diagonal matrix of eigenvalues of $\hat{H}$. Thus, we may write eq 8 as

$$R^X_{pq}(t) = \mathrm{Tr}[\tilde{S}_{Xp} e^{-i\tilde{H}^X t}\, \tilde{S}_{Xq} e^{i\tilde{H}^X t}] = \sum_{m,n} \exp(i\omega^{X_t}_{mn})(\tilde{S}_{Xp})_{mn}(\tilde{S}_{Xq})_{nm} \tag{10}$$

where $\omega^X_{mn} = \hat{H}^X_{mm} - \hat{H}^X_{nn}$. It is expedient to evaluate eq 7 via its Fourier transform

$$\langle \hat{P}^S \rangle(B,\omega) = \frac{1}{4}\delta(\omega) + \frac{1}{M} \sum_{p,q=x,y,z} R^A_{pq}(\omega) * R^B_{pq}(\omega) \tag{11}$$

where * denotes convolution and

$$R^X_{pq}(\omega) = \sum_{m,n} (\tilde{S}_{Xp})_{mn}(\tilde{S}_{Xq})_{nm}\, \delta(\omega + \omega^X_{mn}) \tag{12}$$

Now, in order to solve the field derivative of eq 3 for $f(t)$, it is imperative that we evaluate the singlet probability $\langle \hat{P}^S \rangle$ sufficiently accurately, which in practice means that we must include a realistic number of magnetic nuclei. However, as will be seen shortly, sufficient accuracy can be obtained without calculating the exact spin evolution in what will be a large spin system. We employ a frequency-domain binning procedure to

allow incorporation of sufficient magnetic nuclei using the available computational resources.

To begin, notice that eqs 11 and 12 give the singlet probability as a sum of delta functions with various frequencies (ω_k) and amplitudes (α_k):

$$\langle \hat{P}^S \rangle(B,\omega) = \sum_k \alpha_k(B)\, \delta(\omega - \omega_k(B)) \tag{13}$$

Transforming eq 3 into the frequency domain therefore gives

$$\Phi_S(B) = \int_0^\infty [\sum_k \alpha_k(B)\delta(\omega - \omega_k(B))]F(\omega)\, d\omega \tag{14}$$

where $F(\omega)$ is the Fourier transform of $f(t)$.

We proceed by discretizing eq 14 at a set of field strengths B_i and frequencies ω_j. Provided that we have taken enough frequency samples, $F(\omega)$ will be a piecewise constant around each sample ω_j. Therefore we write

$$\mathbf{s} = \mathbf{AF} \tag{15}$$

where the vector of singlet yields has elements $s_i = \Phi_S(B_i)$, the singlet probability becomes a matrix with elements $A_{ij} = \sum_{k:\omega_k \approx \omega_j} \langle \hat{P}^S \rangle(B_i, \omega_k)$, and the Fourier transform of the re-encounter probability is sampled to give a vector with elements $F_j = F(\omega_j)$. The field strengths are chosen to cover the range of the experimental data which, for ease of analysis, are interpolated linearly, without smoothing, at a resolution of 0.1 mT.

An important consequence of this frequency domain binning procedure is that we need no longer evaluate the $R^X_{pq}(\omega)$ exactly. If we bin the $R^X_{pq}(\omega)$ in the frequency domain before performing the convolution in eq 11, we arrive much more rapidly at the desired singlet probability matrix **A**.

The experimental data are proportional to the derivative of the singlet yield with respect to the magnetic field strength. We differentiate eq 15 approximately by premultiplying by a differentiation matrix **D** giving

$$\mathbf{s}' = \mathbf{Ds} = \mathbf{DAF} \tag{16}$$

In this work, **D** is a fourth-order finite differences matrix, calculated using Fornberg's method.[35] Appropriate one-sided finite difference approximations are used for the terminal points, making use of the symmetry $\Phi_S(B) = \Phi_S(-B)$.

Finally, to allow us to use our physical intuition in respect of the time domain re-encounter probability **f**, we convert **F** back into the time domain using the appropriate inverse discrete Fourier transform, shown here by the matrix $\mathcal{F}^{-1}$,

$$\mathbf{s}' = [\mathbf{DA}\mathcal{F}][\mathcal{F}^{-1}\mathbf{F}] = [\mathbf{DA}\mathcal{F}]\mathbf{f} = \mathbf{Rf} \tag{17}$$

In practice, the matrix **R** is evaluated as a column-wise fast Fourier transform of **DA**, while a row-wise FFT would suffice to convert **F** into **f**.

In preliminary work, we calculated the spin evolution in the [$Py^{\bullet -}$ $DMA^{\bullet +}$] radical pair using a variety of frequency domain binning resolutions and included different numbers of hyperfine coupling constants. Each case was evaluated by plotting the singlet yield derivative determined using $f(t) = k \exp(-kt)$ for the re-encounter probability distribution.[9] It was found that the three groups of equivalent nuclei with the largest hyperfine couplings on each radical (Table 2) could be included within a reasonable computation time. In order to obtain singlet-yield derivative curves that were converged to plotting accuracy for magnetic fields in the range 0−20 mT we found that the number of bins should not be less than ~25 000. In the following, 25 001 bins were used so as to have one centered at zero frequency. Although this calculation of the matrix **R** is lengthy, it need only be performed once for any given radical pair and set of magnetic field values.

Thus, **R** has dimension 201 × 25 001 corresponding, via eq 17, to 201 data points and 25 001 samples of $f(t)$, which are evenly distributed over times $t = 0 \rightarrow 5000\pi$ ns. However, in work with both synthetic and experimental data, we found no reasonable solution for $f(t)$ that had significant amplitude beyond 100 ns. In order to improve the speed of data analysis, we assume that $f(t) = 0\ \forall\ t \geq 80\pi$ ns. When applied to eq 17, this assumption amounts to truncating **f** after 400 elements and deleting all but the first 400 columns of **R**. Results obtained using the regularization methods described below with both the full **R** and the reduced **R** are almost indistinguishable. The reduced **R** has consequently been used in all the reconstructions presented below.

5. Regularization

From the form of eq 17 it would appear that we are very near to finding the empirical re-encounter probability distribution that we seek. However, there are 25 001 (or 400 in the simplified case) values of $f(t)$ in **f** which must be determined from 201 experimental data points in **s′**. Such underdetermined problems are very common, and linear solvers (e.g., the "backslash" solver built into Matlab[36]) are designed to find an optimal solution in a least-squares sense, namely

$$\mathbf{f_{LS}} = \underset{\mathbf{f}}{\operatorname{argmin}} \left\| \mathbf{Rf} - \mathbf{s}' \right\|_2 \tag{18}$$

Unfortunately, when this solution $\mathbf{f_{LS}}$ is examined it is found to be both highly oscillatory and dominated by numerical noise. The problem is not just underdetermined; it is ill-posed. In other words, the recovered solutions $\mathbf{f_{LS}}$ are very sensitive to errors in the data **s′** and in the matrix **R**, to the extent that accumulated rounding errors are enough to render the recovered $\mathbf{f_{LS}}$ meaningless. The ill-posed nature of the problem manifests itself in other ways too. For example, we initially attempted to invert the continuous form of this problem, the derivative of eq 3, by model fitting. Having chosen a trial functional form for $f(t)$, we attempted to fit a set of parameters. Yet, because the problem is ill-posed, there were a great many local minima among the parameters, and it proved impossible to optimize the model properly.

Fortunately, such ill-posed, underdetermined problems occur frequently throughout the physical sciences, and powerful "regularization methods" have been developed for their solution.[37] Here we use two such approaches which were first tested using synthetic data (see Supporting Information) and which we now apply to the experimentally determined magnetic field effect data.

(35) Fornberg, B. *Math. Comput.* **1988**, *51*, 699−706.

(36) *Matlab*, R2006a; The Mathworks, Inc.

(37) Hansen, P. C. *Rank-deficient and discrete ill-posed problems: numerical aspects of linear inversion*. SIAM: 1998.

5.1. Tikhonov Regularization. Tikhonov regularization is one of the simplest and best known linear regularization methods.[38,39] We introduce two measures of the quality of a solution: the residual norm $\left\|\mathbf{Rf} - \mathbf{s}'\right\|_2$ measures the failure of the solution to reproduce the data, while the solution norm $\left\|\mathbf{Lf}\right\|_2$ measures the deviation of the solution from some expected form (typically based on physical insight). The Tikhonov solution is

$$\mathbf{f_T} = \underset{\mathbf{f}}{\operatorname{argmin}} \left\|\mathbf{Rf} - \mathbf{s}'\right\|_2 + \lambda\left\|\mathbf{Lf}\right\|_2 \qquad (19)$$

The regularization parameter λ allows us to choose how rigidly to impose our prior knowledge on the solution. A very large value of λ produces a solution which has little connection to the data but which will conform to our prior knowledge, while a very small value of λ will not produce sufficient damping of the troublesome oscillatory components and will therefore give way to noisy solutions. In the limit $\lambda \rightarrow 0$, eq 19 tends to eq 18 and the Tikhonov solution $\mathbf{f_T}$ tends to the least-squares solution $\mathbf{f_{LS}}$. We choose an optimal value for λ using the "L-curve" method[37,40,41] (see Supporting Information).

The regularization matrix $\mathbf{L}$ is chosen to select the unwanted components in a solution, which are then penalized by the second term in eq 19. In this work, we have used either $\mathbf{L}$ equal to the identity matrix, which tends to reduce the recovered $f(t)$ to zero wherever possible, or $\mathbf{L}$ equal to a second derivative finite-differences matrix $\mathbf{D}_2$, which tends to produce smooth $f(t)$ by penalizing regions with large changes in gradient. Both choices penalize the highly oscillatory behavior seen in the unregularized solutions.

In addition to these preferences for nonoscillatory solutions, we know that $f(t)$ must be non-negative because it is a probability distribution. It would seem sensible to solve eq 19 subject to the constraint that $\mathbf{f_T} \geq 0$. It may be shown[37] that eq 19 can be solved by finding the constrained least-squares solution to the normal equation:

$$[\mathbf{R}^\dagger\mathbf{R} + \lambda^2\mathbf{L}^\dagger\mathbf{L}]\mathbf{f_T} = \mathbf{R}^\dagger\mathbf{s}' \qquad :\mathbf{f_T} \geq 0 \qquad (20)$$

In the following work, we solved the unconstrained problem in eq 19 using the tikhonov.m code in Hansen's Matlab toolbox.[42] For the constrained problem in eq 20 we used the fast non-negative least-squares (FNNLS) algorithm proposed by Bro and Jong,[43] which is a more efficient implementation of the classic NNLS algorithm of Lawson and Hansen.[44] Again, calculations were performed in Matlab.

5.2. Maximum Entropy Regularization. An alternative, nonlinear, Bayesian regularization method is known as the maximum entropy method[45−49] (often abbreviated as MEM or MaxEnt). In its classic form, the algorithm aims to recover, from among all the solutions consistent with the experimental data, the most probable or maximum likelihood solution $\mathbf{f_{ME}}$. As before, consistency means that $\mathbf{Rf_{ME}} \approx \mathbf{s}'$ as measured by an appropriate statistic. In practice, this maximum likelihood solution is determined by maximizing the entropy

$$S = -\sum_k \left(\frac{(f_{\mathrm{ME}})_k}{b}\right) \ln\left(\frac{(f_{\mathrm{ME}})_k}{b}\right) \qquad (21)$$

subject to a chi-squared test

$$\chi^2 = \sum_k [(\mathbf{Rf_{ME}})_k - s'_k]^2/\sigma^2 = \chi^2_{\mathrm{target}} \qquad (22)$$

where b is a baseline parameter, σ is (an estimate of) the standard deviation of the experimental noise, and χ^2_{target} is equal to the number of data points in $\mathbf{s}'$ (201 here).[45,49]

In this formulation, the baseline factor b is the principal regularization variable. If the data do not constrain the solution at a particular point, then the maximum entropy method will choose $f^*_{\mathrm{ME}} = be^{-1}$ for the re-encounter probability there. When the solution is constrained by the data, b governs the relative penalty for increasing f at that point. For a re-encounter probability value $(f_{\mathrm{ME}})_k > be^{-1}$, the entropy penalty will increase more rapidly the smaller b is. Thus, smaller values of b will pull the baseline down more aggressively and give sharper peaks, while larger values of b will result in broader peaks and a higher baseline. The choice of the optimal value of b is discussed in the Supporting Information.

In this work, we use an algorithm described by Skilling and Bryan[50] to solve the nonlinear constrained optimization problem defined by eqs 17, 21, and 22. This algorithm uses a suitable subspace of search directions based on the entropy S and the constraint χ^2 with a metric for optimization based on the entropy S. All calculations were performed in Matlab, based on the original Fortran code kindly supplied by G. J. Daniell (University of Southampton).

6. Quantitative Analysis of Magnetic Field Effects

Having established that the two regularization methods are able to recover the re-encounter probability $f(t)$ from a variety of synthetic data (see Supporting Information), we proceed to apply them to the experimental data shown in Figure 1. In both cases, the regularization parameters were chosen after a careful evaluation using the synthetic data (see Supporting Information).

Tikhonov regularization was applied to the data for each isotopomer combination taken separately. We obtained the most satisfactory results by using $\mathbf{L} = \mathbf{D}_2$ for the solution seminorm, which discourages oscillations in the recovered $f(t)$, by constraining $f(t) \geq 0$ using the FNNLS algorithm and by choosing λ using the L-curve method. The results are given in Figure 2A and discussed below.

Maximum entropy regularization was also applied to each isotopomer combination taken separately. Figure 2B shows the recovered $f(t)$, which is discussed below. One difference between

(38) Tihonov, A. N. *Soviet Math. Dokl.* **1963**, *4*, 1035−1038.
(39) Tikhonov, A. N.; Arsenin, V. Y. *Solutions of ill-posed problems*. V. H. Winston & Sons: Washington, D.C., 1977.
(40) Hansen, P. C. *SIAM Review* **1992**, *34*, 561−580.
(41) Hansen, P. C.; O'Leary, D. P. *SIAM J. Sci. Comput.* **1993**, *14*, 1487−1503.
(42) Hansen, P. C. Regularization tools: a Matlab package for analysis and solution of discrete ill-posed problems.
(43) Bro, R.; de Jong, S. *J. Chemomet.* **1997**, *11*, 393−401.
(44) Lawson, C. L.; Hanson, R. J. *Solving least squares problems*; Prentice Hall Inc.: Englewood Cliffs, NJ, 1974.
(45) Gull, S. F.; Daniell, G. J. *Nature* **1978**, *272*, 686−690.
(46) Jaynes, E. T. *Phys. Rev.* **1957**, *106*, 620−630.
(47) Jaynes, E. T. *Phys. Rev.* **1957**, *108*, 171−190.
(48) Jaynes, E. T. In *Maximum Entropy Formalism Conference*; Levine, R. D., Tribus, M., Eds.; MIT Press: 1978; pp 15−118.
(49) Buck, B.; Macaulay, V. A. *Maximum Entropy in Action*; Oxford University Press: Oxford, 1991.
(50) Skilling, J.; Bryan, R. K. *Mon. Not. R. Astron. Soc.* **1984**, *211*, 111−124.

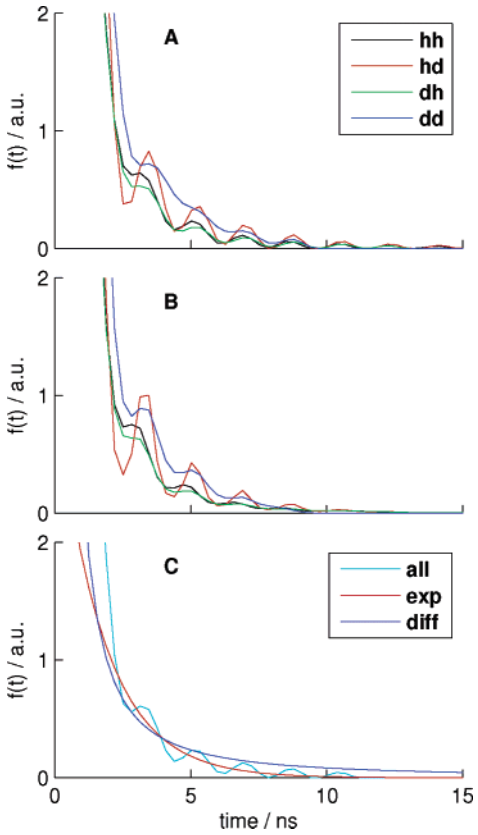

Figure 2. Best recovered $f(t)$ for (A) Tikhonov regularization and (B) maximum entropy regularization for each of the four isotopomer combinations. (C) Tikhonov regularization recovery of a single $f(t)$ to fit all four isotopomer combinations simultaneously. For (C), the experimental data for each isotopomer combination were scaled as part of the regularization procedure. The optimal scaling factors were as follows: **hh** 1.00 (i.e., not rescaled), **hd** 0.73, **dh** 1.08, **dd** 0.59. (C) also contains the best fit of the recovered $f(t)$ at $t > 2$ ns to an exponential (red, $k = 5.8 \times 10^8$ s^{-1}) and to the diffusion model (blue, $f(t) \propto t^{-3/2}$).[19,20] In all cases, the fits to the experimental data were exemplary. The fits for case (A) are shown in Figure 3. (See Supporting Information for the remaining fits to the data, selected Tikhonov L-curves, and further information.)

the tests using synthetic data and the analysis of the experimental data was the choice of noise standard deviation estimate σ. In order to obtain convergence with the experimental data, it was necessary to increase σ slightly from the value estimated by inspection of the raw data at fields higher than the saturation value. This discrepancy might arise because of the use of a lock-in amplifier, which causes the noise to be correlated somewhat between neighboring data points, something that is not included in our maximum entropy treatment. It could also arise from the neglect of some of the small hyperfine couplings or other interactions. Nevertheless, evaluation with synthetic data shows that increasing the noise estimate slightly has only a small effect on the recovered $f(t)$. Hence, this point should not concern us further.

The $f(t)$ distributions for the four isotopomer combinations (Figure 2A and B) are strikingly similar to one another for values of t greater than 2 ns. To test whether they are truly equivalent, we attempted to recover a single $f(t)$ by processing all four isotopomer combination data sets simultaneously. Very satisfactory fits to the data were obtained by allowing a modest constant scaling of each data set relative to **hh**. Physically, this corresponds to dropping our assumption of exactly identical experimental conditions (e.g., concentrations, light intensity, detector performance, sample temperature) for the four isotopomer combinations. The combined analysis was accomplished by wrapping an outer nonlinear least-squares minimization routine around the Tikhonov regularization code. In the outer routine, the relative intensities of the data sets are varied in order to minimize the residual norm. This process was repeated for each value of λ in order to construct an L-curve from which the optimal λ was obtained, giving the result presented in Figure 2C.

Before interpreting the re-encounter probability distributions in Figure 2, two technical points need to be mentioned. First, we observed that the data for the **dd** isotopomer were somewhat more difficult to analyze than those from the other isotopomer combinations. This is reflected in the slightly higher maximum entropy noise estimate required for the **dd** analysis in Figure 2B. During our evaluation with synthetic data, it was also found to be more difficult to reconstruct $f(t)$ from the **dd** isotopomer combination. Since these difficulties arise even with synthetic data, they are not caused by deficiencies in the theoretical model or by experimental difficulties. Instead, it seems that the particular hyperfine coupling constants in the **dd** isotopomer combination create an inversion problem that is even more severely ill-posed than those for the other isotopomer combinations. Second, there are noticeable residual oscillations in the $f(t)$ functions obtained by all three methods (Figure 2). These are almost certainly spurious since their positions and amplitudes depend on the choice of regularization parameter (b for maximum entropy and λ for Tikhonov regularization). They demonstrate one of the fundamental tendencies of ill-posed problems, which tend to introduce unphysical oscillations into the solution when even very tiny amounts of noise are present in the data.[37] Thus, attempts to solve eq 18 in a least-squares sense (not shown) gave "solutions" with such wild oscillations that any physically meaningful information on the re-encounter probability was completely obscured. Regularization methods dramatically improve this situation and allow many of the oscillations to be eliminated. Nevertheless, there are fundamental limits to the information contained in experimental data such as those in Figure 2. We should not expect to achieve a perfect suppression of oscillatory artifacts in an ill-posed problem.

7. Discussion

The re-encounter probability distributions $f(t)$ for the four isotopomer combinations are remarkably similar to one another for times longer than ~2 ns. This can be seen in Figure 2A and B and is perhaps most powerfully demonstrated by Figure 2C, where a single $f(t)$ was recovered from data for all four isotopomeric reactions simultaneously. The close fit to the experimental data (see Figure 3 and the Supporting Information) provides direct evidence that diffusion and reaction kinetics in these aromatic radical ion pairs are changed very little by perdeuteration. Isotopic substitution is clearly an effective means of modifying the hyperfine interactions and hence the extent and efficiency of S ↔ T interconversion in a radical pair reaction without disturbing other parameters; this bodes well for future studies.

We also note the strong resemblance of the $f(t)$ distributions recovered from the Tikhonov (Figure 2A) and maximum entropy (Figure 2B) methods. The former is a linear regularization method, while the latter is nonlinear. That these two disparate

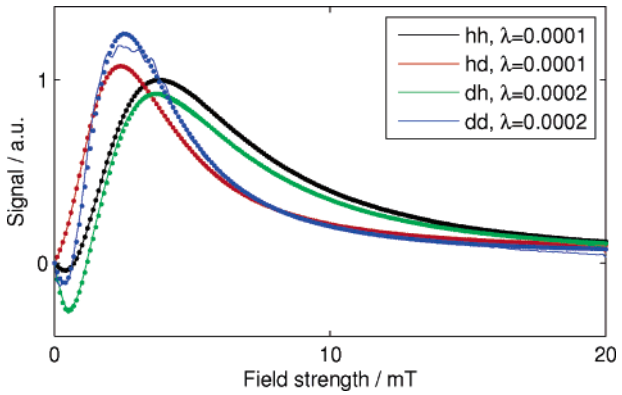

Figure 3. Fits (lines) to the experimental data (dots) for Tikhonov regularization corresponding to the recovered $f(t)$ in Figure 2A. Optimal values of the regularization parameter λ, chosen according to the L-curve method, are given in the legend for each isotopomer combination.

techniques yield the same re-encounter probability distributions (for $t > 2$ ns) significantly strengthens our confidence that the $f(t)$ shown above are to be believed. It seems quite implausible that two independent methods should both fail in the same manner. This confidence is increased still further by the robust behavior of the two approaches when working with synthetic data.

Although the re-encounter probabilities obtained from Tikhonov and maximum entropy regularization are rather similar, there are substantial differences in the first 2 ns (not shown in Figure 2). The Tikhonov $f(t)$ is essentially linear in t for $t < 2$ ns with a large negative gradient. The $f(t)$ from maximum entropy, however, tends to the value of the baseline parameter b as $t \rightarrow 0$ ns. This contrasting behavior is expected if $f(t < 2$ ns$)$ is not constrained by the experimental data; i.e., if the re-encounters that occur during the first 2 ns make little contribution to $d\Phi_S(B)/dB$. As discussed in connection with eqs 19 and 20, the use of $\mathbf{L} = \mathbf{D}_2$ in Tikhonov regularization disfavors oscillations and so will produce an $f(t)$ with a vanishing second derivative; similarly, in the absence of a significant χ^2 constraint, the form of the expression for S (eq 21) causes the maximum entropy reconstruction to be pulled strongly toward the value of the baseline parameter b. This situation is consistent with the contribution to the singlet yield during the period $0 < t < 2$ ns being independent of the magnetic field strength to a good approximation. Thus, the data, which are proportional to $d\Phi_S(B)/dB = 0$, do not constrain $f(t)$ at these short times. In the Supporting Information, Figure S6 shows a plot of the standard deviation of the singlet probability over the 201 different field strengths which supports this conclusion.

This argument sheds light on the interpretation of the $f(t)$ distributions recovered from the magnetic field effect data. The results in Figure 2 do not represent the total distributions of re-encounter probabilities, but rather the distributions of the re-encounters *that are important for the formation of a magnetic field effect*. It is evident from Figure 2 that these re-encounters occur principally between about 2 and 10 ns. The large number of re-encounters that are expected to take place during the first 2 ns are unimportant because 2 ns is too short a time to allow significant spin evolution of the radical pair under the Zeeman interaction. For applied magnetic fields in the range $0 < B < 20$ mT, the electron Zeeman interaction has a maximum frequency of ~560 MHz, whose reciprocal is ~2 ns. Since $d\Phi_S(B)/dB$ is expected to have its maximum value at $B \approx B_{1/2} \approx 5$ mT ≈ 140 MHz, we can anticipate that the optimum time for re-encounters will be approximately (1/140) MHz ≈ 7 ns, as found in the recovered $f(t)$ functions in Figure 2.

We may speculate on a further aspect of the interpretation of the $f(t)$ distributions in Figure 2. Hitherto we have chosen to ignore the exchange interaction between the two radicals, certainly a good approximation when the radical−radical separation is large (>1.0−1.5 nm). However, when the radicals are close enough that the exchange dominates the hyperfine and Zeeman interactions, all S ↔ T interconversion ceases and the pair is locked into an S or a T eigenstate. We may therefore think of an "exchange zone" of radical−radical separations (extending out to 1.0−1.5 nm) in which there is no dependence of the radical pair spin evolution on the applied magnetic field. Thus, during a diffusive trajectory, S ↔ T interconversion can be considered to start only when the radicals leave the exchange zone and to stop as soon as they re-enter it. Any radical pair that re-enters in an S state remains in an S state until it either recombines or diffuses apart again. Thus, the recovered $f(t)$ may be regarded as giving information on the trajectories that are important for the generation of the magnetic field effect, i.e., those that spend 2−10 ns outside the exchange zone. The fact that all the $f(t)$ distributions in Figure 2 have a very low amplitude beyond 10 ns simply reflects the low probability that the radicals return to the exchange zone after such a relatively long time.

There are clear parallels here with the production of electron and nuclear magnetic polarizations (CIDEP and CIDNP) by the RPM[19,20,23] which also require the radicals to undergo a period of exchange-free diffusion. However, there are sufficient differences between the origins of high-field CIDEP/CIDNP and the LFE that it cannot automatically be assumed that the dependence on the magnetic properties of the radicals and their diffusive trajectories will be identical. For example, the exchange interaction plays different roles in the generation of CIDEP and of MFEs: without exchange there can be no electron spin polarization. MFEs, by contrast, are clearly influenced by exchange interactions (see, e.g., Supporting Information, section 7), but they do not disappear in the absence of exchange. Another qualitative difference is that without spin-selective reactivity there can be no MFE, while a geminate spin-correlated radical pair can lead to electron spin polarization even if the radicals are infinitely long-lived. Finally, there are differences in the importance of the various magnetic interactions within the radicals. Assuming the two radicals have identical g-values (as here), the parameter that controls the frequency of singlet−triplet interconversion at high field, and therefore determines the size and properties of the CIDEP, is the difference in EPR frequencies of the two radicals.[19,20,23] This parameter depends exclusively on the hyperfine coupling constants when $\Delta g = 0$. For low-field MFEs, the situation is more complex. The corresponding singlet−triplet mixing frequency depends in a much more complicated way on the hyperfine coupling constants, as well as on the electron Zeeman interaction. In light of this, it is not clear that the time scale of re-encounters that are important for high field CIDEP/CIDNP should be identical to that determined here for the LFE or MFEs. Further work will be needed to clarify this matter.

Finally, we observe that the decaying $f(t)$ distribution ($t >$ 2 ns) in Figure 2 resembles that assumed in the traditional

exponential model[9] (with a best-fit rate constant $k = 5.8 \times 10^8$ s^{-1}; see Figure 2C). The agreement with the diffusion model[20] is less satisfactory principally because the predicted $t^{-3/2}$ dependence seriously overestimates the extent of the "tail" of the $f(t)$ distribution after about 6 ns (also shown in Figure 2C). The failure of the diffusion model here is very likely due to the influence on the motion of the radical ions of their mutual Coulombic attraction (the Onsager distance in the DMF/THF solvent mixture is approximately 4 nm). The exponential model, in spite of its apparent crudity, evidently captures the general behavior of the re-encounters on which the magnetic field effects depend. Our data therefore support the use of such empirical diffusion models for the calculation of magnetic field effects.

Acknowledgment. We thank the EPSRC, the EMF Biological Research Trust, the Royal Society, and INTAS for financial support; the Oxford Supercomputer Centre for computer time used in developing the LFE depth and $B_{1/2}$ rules of thumb; Dr. D. V. Stass for helpful discussions; Mr. J. Lillington for additional measurements; and Mr. M. Gatenby, Dr. P. Kukura and Dr. P. D. McKeating for preliminary work.

Supporting Information Available: Evaluation of regularization methods using synthetic data. Examples of maximum entropy and Tikhonov fits. Monte Carlo radical pair calculations. Validation of eq 3. This material is available free of charge via the Internet at http://pubs.acs.org.

JA068209L